IEEE Access
Multidisciplinary | Rapid Review | Open Access Journal

Received December 4, 2017, accepted January 7, 2018, date of publication January 12, 2018, date of current version March 12, 2018.

Digital Object Identifier 10.1109/ACCESS.2018.2792442

A New fMRI Informed Mixed-Norm Constrained Algorithm for EEG Source Localization

HAILING WANG[1], XU LEI[2], ZHICHAO ZHAN[3], LI YAO[1], AND XIA WU[1,4]

[1]College of Information Science and Technology, Beijing Normal University, Beijing 100875, China
[2]Sleep and NeuroImaging Center, Faculty of Psychology, Southwest University, Chongqing 400715, China
[3]State Key Laboratory of Cognitive Neuroscience and Learning, Beijing Normal University, Beijing 100875, China
[4]State Key Laboratory of Networking and Switching Technology, Beijing University of Posts and Telecommunications, Beijing 100088, China

Corresponding author: Xia Wu (wuxia@bnu.edu.cn)

This work was supported in part by the General Program of National Natural Science Foundation of China under Grant 61571047, in part by the Fundamental Research Funds for the Central Universities under Grant 2017EYT36, and in part by the Open Project Funding of the State Key Laboratory of Networking and Switching Technology, Beijing University of Posts and Telecommunications under Grant SKLNST-2013-1-03.

ABSTRACT Complementary with electroencephalograph (EEG), functional magnetic resonance imaging (fMRI), with high spatial resolution, is powerful at providing prior source locations based on actual brain physiology. It hereby can help improve the accuracy of EEG source localization. However, most of the current methods directly penalize the sources whose fMRI activation probability is low and estimate the sources activities at every time point. Thus, they do not account for the temporal interrelated and non-stationary features of electromagnetic brain signals, and some are too much dependent on the fMRI prior. Here, we propose a new fMRI informed EEG source localization method and is termed fMRI-informed spatio-temporal unifying tomography (FIST). It uses a mixed norm constraint defined in terms of time–frequency decomposition of the sources and combines it with fMRI prior. The Fast Iterative Shrinkage Thresholding Algorithm is employed to solve the optimization problem. Both simulated and real EEG data are applied to assess the performance of the proposed method. Compared with L2-norm constrained methods, FIST has the superiority brain source estimation both in the spatial and temporal domains. By virtue of the fMRI information as a prior, FIST has great improvement in spatial accuracy and computational efficiency, when comparing with the method which only uses mixed-norm constraint. In addition, FIST shows good ability to select the fMRI priors to get a better estimation without totally depending on the prior, when comparing with the method which also has fMRI prior information.

INDEX TERMS Source localization, EEG, fMRI, mixed-norm constraint, inverse problem.

I. INTRODUCTION

As a popular noninvasive technology to measure brain activity, the electroencephalograph (EEG) has been applied to measure the dynamic processes in the brain with great temporal resolutions of milliseconds [1], [2]. Due to the limitation of the number of measurement sensors, EEG has poor spatial resolution [3]. However, source localization with EEG can overcome this drawback, which reconstructs brain activities with high temporal and good spatial resolution [3], [4]. The reconstructed brain activities are also known as source currents, which located everywhere in the brain [5]. Such EEG source localization technique has been widely used in disease diagnostics [6], [7] and in cognitive research [8], [9].

At present, there are two main methodological categories for solving the EEG source localization problem [10]: (i) the dipole fitting method of which attempts to estimate brain source activities with a small number of equivalent current dipoles [11] and (ii) the distributed method of which estimates the brain sources activities using a large number of dipoles that encompass the whole cortical surface [12]. Since the distributed methods assume that thousands of dipole sources are distributed in the brain cortical surface while an order of magnitude fewer scalp sensors are used to record the EEG signal, the EEG source localization problem is ill-posed [13]. Therefore, constraints based on the characteristics of the actual source distribution are essential for solving the problem [14]. One common constraint is the L2-norm, which measures the overall energy of the sources. This type of methods includes the minimum norm estimate (MNE) [15], weighted MNE (wMNE) [16], and

low-resolution electromagnetic tomography (LORETA) [17], along with the family members exact LORETA (eLORETA) [18] and standardized LORETA (sLORETA) [19]. Another is sparse constrained methods, including the L1-norm constraint [20] and sparsity-inducing norm afforded by empirical Bayes (such as Sparse Bayesian learning (SBL) [21] and Multiple Sparse Priors (MSP)) [22]. Nevertheless, L2-norm constrained methods usually overestimate the source spatial extent, so that cannot distinguish multi-patch sources [23]; while sparse constrained methods may lead to over-focal or scattered estimation, which contain activations at fewer cortical regions than actual sources [24].

Both the L2-norm and sparse constrained methods are implemented separately at each time point leading to non-smooth and noise sensitive source time course estimation [25], [26]. They merely take into account the spatial characteristics of the sources, without considering the fact that the activities related to EEG measurements are spatially and temporally interconnected [27]. Hence, several studies try to combine spatial and temporal constraint as regularization term in source localization problem. For instance, a random-walk dynamical model with Laplacian spatial constraints is used to describe the dynamics of EEG source currents [28]. The spatio-temporally regularized algorithm for M/EEG patch image (STRAPS) [26] and dynamic maximum a posteriori expectation maximization (dMAP-EM) [29] use a nearest-neighbor multivariate autoregressive (MVAR) model to formulate the spatio-temporal connections. However, the implicit assumption of these methods is that the sources are stationary, which is only suitable for short time intervals [25]. Indeed, multiple transient sources are sequentially activated during the EEG analysis period, in other words, brain source signals are transient and non-stationary [30].

The presence of the source non-stationarity is due to many reasons, such as epileptogenic transients [31], physiological and instrumental artifacts [32]. Evoked brain activity, on the other hand, reflects event related non-stationary phenomena [33]. Time-frequency mixed-norm estimates (TF-MxNE) [25] and spatio-temporal unifying tomography (STOUT) [34] address these transient and non-stationary characteristics by a sparse set of time-frequency basis functions (atoms). TF-MxNE obtains the frequency domain representation from the time-series data using the Gabor transform, uses a composite regularizer which is the sum of the L21-mixed-norm and L1-norm. While the TF-MxNE solutions are not composed of smooth activation patches. As a remedy, STOUT imposes a spatial basis function [35] constraint at each modeled dipole location. However, the constraints are not based on actual brain physiology, and it may leads to biased and plausible solutions. Another disadvantage is that due to the source time-frequency decomposition, STOUT requires a great amount of computational time and memory consumption.

The functional magnetic resonance imaging (fMRI) is another widely used non-invasive neuroimaging technique with a high spatial resolution of millimeters [36] and is useful for providing prior source locations based on actual brain physiology in EEG source localization [36]–[38]. Based on the hierarchical linear model, the covariance derived from fMRI data has been proposed to improve the spatial accuracy of EEG source localization [39], [40]. This model was further improved in the L2 minimum norm estimation with a subspace regularization term of fMRI-defined subspace [41], or with a functional area constrained estimator (FACE), which was derived from a segmentation of the cortex into areas defined by retinotopic maps of the visual field or by functional localizers obtained independently by fMRI [42]. However, most of the previous models were developed for a single time-point, based on the adaptive Wiener filter, and estimate the source covariance matrix by combining the quantified fMRI responses with the segmented EEG signals before response averaging [43], [44]. Some researchers take advantage of the spatial alignment between neural and vascular activities to reduce ambiguity [36], or consider the source variance at each location as an unknown parameter, which depends on the fMRI activity [14], [45], based on Bayesian estimation. These techniques suggested that utilizing the fMRI information as a prior in different ways is feasible and effective for EEG source localization [46]. However most of these methods estimate source activity at each time-point, they do not take temporal interrelated features of electromagnetic brain signals into account, or are too dependent on the fMRI prior.

Motivated by previous studies [25], [34], [39], [46], this paper develops a new method based on STOUT, which introduces fMRI prior in the EEG source localization and is termed fMRI-informed spatio-temporal unifying tomography (FIST). Unlike previous methods [39]–[41], [45] that directly penalize the EEG sources whose fMRI-derived activation probability are low [47], FIST uses a mixed norm constraint, which is defined in terms of the time-frequency decomposition of the sources, and combines it with fMRI prior. Thus, this can avoid direct penalization of the EEG sources and estimate source activity at every time-point. The Fast Iterative Shrinkage Thresholding Algorithm (FISTA) [48], [49] is employed to solve the optimization problem. To assess the performance of the proposed method, we compared it with the classical L2-norm constrained methods (LORETA, wMNE), mix-norm constrained method (STOUT), and fMRI informed method dynamic Statistical Parameter Mapping (dSPM) [39]. We first validated the methods on simulated datasets, and then applied them to a realistic human EEG dataset.

II. MATERIALS AND METHODS

A. FMRI INFORMED SPATIO-TEMPORAL UNIFYING TOMOGRAPHY

We now describe the mathematical formulation of the source localization problem. Based on the quasi-static approximation of Maxwell's equations, the relationship between the

observed EEG signals and the source currents is described by the following linear function [50]

$$\mathbf{Y} = \mathbf{L}\mathbf{J} + \boldsymbol{\varepsilon} \tag{1}$$

where $\mathbf{Y} \in \mathbb{R}^{N_c \times N_t}$ denotes the observed EEG signals on the scalp from N_c sensors, sampled at N_t time points. $\mathbf{J} \in \mathbb{R}^{3N_d \times N_t}$ is the source current density matrix of N_d dipolar electrical brain sources with three unknown dipole moments at the N_t time points. $\mathbf{L} \in \mathbb{R}^{N_c \times 3N_d}$ is the lead field matrix composed as $\mathbf{L} = (\mathbf{L}^x, \mathbf{L}^y, \mathbf{L}^z)$ where $\mathbf{L}^{x/y/z}$ are lead fields of the current sources in each direction x, y and z, respectively. $\boldsymbol{\varepsilon} \in \mathbb{R}^{N_c \times N_t}$ is the Gaussian distributed noise with covariance $\mathbf{Q}_{\boldsymbol{\varepsilon}} \in \mathbb{R}^{N_c \times N_c}$, which can be estimated from pre-stimulus data, or simply set to the identity matrix. We applied the latter approach in this study [10].

The goal of the source localization is to estimate $\mathbf{J}$. We now describe our proposed algorithm FIST, which extends STOUT [34], to solve it. The objective function of STOUT is given by

$$\mathbf{C}^* = \arg\min_{\mathbf{C}} \left\{ \|\mathbf{Y} - \mathbf{L}\left(\boldsymbol{\Phi}_{\mathbf{s}} \otimes \mathbf{I}_{\mathbf{3}}\right)\mathbf{C}\boldsymbol{\Phi}_{\mathbf{t}}\|^2_{Q_\varepsilon} + \lambda_s \|\mathbf{C}[i,\cdot]\|_{21} + \lambda_t \|\mathbf{C}\|_1 \right\} \tag{2}$$

where the current density $\mathbf{J} = \mathbf{C}\boldsymbol{\Phi}_{\mathbf{t}}$ is decomposed into temporal basis functions $\boldsymbol{\Phi}_{\mathbf{t}}$ and the corresponding coefficients $\mathbf{C}$ by time-frequency decomposition. The matrix $\boldsymbol{\Phi}_{\mathbf{s}} \in \mathbb{N}^{N_d \times N_d}$ represents the spatial basis functions, $\mathbf{I}_{\mathbf{3}} \in \mathbb{N}^{3\times 3}$ is an identity matrix, and $\otimes$ is the Kronecker product. λ_s and λ_t are the parameters to be estimated. After the coefficients $\mathbf{C}$ are obtained by solving equation (2), the estimated source can be given by $\hat{\mathbf{J}} = \mathbf{C}\boldsymbol{\Phi}_{\mathbf{t}}$.

Similar to the representation in STOUT, the objective function of FIST can be written as

$$\mathbf{C}^* = \arg\min_{\mathbf{C}} \left\{ \|\mathbf{Y} - \mathbf{L}\left(\boldsymbol{\Phi}_{\mathbf{s}} \otimes \mathbf{I}_{\mathbf{3}}\right)\mathbf{C}\boldsymbol{\Phi}_{\mathbf{t}}\|^2_{\mathbf{Q}_{\boldsymbol{\varepsilon}}} + \sum_{i=1}^{3N_d} \mathbf{w}[i]\left(\lambda_s \|\mathbf{C}[i,\cdot]\|_{21}\right) + \lambda_t \|\mathbf{C}\|_1 \right\} \tag{3}$$

where $\mathbf{w}[i]$ represents the i^{th} source weighting. The spatial basis function is defined as $\boldsymbol{\Phi}_{\mathbf{s}}(i,j) = \exp\left\{-d_g\left\{x_i, x_j\right\}^2/\sigma^2\right\}$, where $d_g\left\{x_i, x_j\right\}$ refers to the geodesic distance between the i^{th} and the j^{th} dipole along the cortical surface. The parameter σ refers to the spatial width of the Gaussians. For the coefficients $\mathbf{C}$, it's obtained using short-time Fourier transform (STFT) [51], and can be defined as $\mathbf{C}(m,n) = \sum_l f(l)\, e^{-2\pi imb(l-an)/L} g(l-an)$, where $f(l)$ is the input signal at time l, $g(\cdot)$ is the modulated window, b is the length of the frequency shift, and a is the length of the time shift. For the parameter a and b, we use the same values as in [34].

FISTA is employed to solve the objective function equation (3). Before applying FISTA, It needs to compute the proximity operator of the weighted $\ell_{21} + \ell_1$ norm:

$$\begin{aligned}\mathbf{C} &= prox_{\ell_{21}+\ell_1}(\mathbf{G}, \lambda_s, \lambda_t) \\ &= \arg\min_{\mathbf{C}} \frac{1}{2}\|\mathbf{G} - \mathbf{C}\|_2^2 + \sum_{i=1}^{k} \mathbf{w}[i]\left(\lambda_s \|\mathbf{C}[i,\cdot]\|_{21}\right) \\ &\quad + \lambda_t \|\mathbf{C}[i,\cdot]\|_1 \end{aligned} \tag{4}$$

where $\mathbf{G} = \mathbf{C} + \mu\left(\boldsymbol{\Phi}_{\mathbf{s}} \otimes \mathbf{I}_{\mathbf{3}}\right)^T \mathbf{L}^T \left(\mathbf{Y} - \mathbf{L}\left(\boldsymbol{\Phi}_{\mathbf{s}} \otimes \mathbf{I}_{\mathbf{3}}\right)\mathbf{C}\boldsymbol{\Phi}_{\mathbf{t}}\right)\boldsymbol{\Phi}_t^H$, $\boldsymbol{\Phi}_t^H$ denotes the Hermitian transpose of $\boldsymbol{\Phi}_t$ [25], $0 < \mu < L^{-1}$, L is the Lipschitz constant. Each coordinate element $\mathbf{C}_{k,p}$ is given by

$$\mathbf{C}_{k,p} = \frac{\mathbf{G}_{k,p}}{|\mathbf{G}_{k,p}|}\left(|\mathbf{G}_{k,p}| - \lambda_t\right)_+ \left(1 - \frac{\lambda_s\sqrt{\mathbf{w}[k]}}{\sqrt{\sum_p \left(|\mathbf{G}_{k,p}| - \lambda_t\right)_+^2}}\right)_+ \tag{5}$$

For calculation convenience, it can also be simplified as

$$\begin{aligned} \tilde{\mathbf{C}}_{k,p} &= \mathbf{G}_{k,p}\left(1 - \frac{\lambda_t}{|\mathbf{G}_{k,p}|}\right)_+ \qquad (a) \\ \mathbf{C}_{k,p} &= \tilde{\mathbf{C}}_{k,p}\left(1 - \frac{\lambda_s\sqrt{\mathbf{w}[k]}}{\left\|\tilde{\mathbf{C}}_{k,p}\right\|_2}\right)_+ \qquad (b) \end{aligned} \tag{6}$$

with $(a)^+ = \max(a, 0)$. The pseudo code for FIST optimization is provided in Algorithm 1. If the value of $\mathbf{w}[i]$ is small, the penalty for the i^{th} source will be small, which means the i^{th} source is likely to be selected as a candidate source. Farther mathematical details and implementation of FISTA can be found in [48] and [49].

TABLE 1. FISTA algorithm used to compute the FIST.

Algorithm 1: FISTA

Initialization: $\mathbf{Z}^{(0)}=0$, with all-zeros matrix $\mathbf{Z} \in \mathbb{C}^{3N_d \times N_f}$, $\mathbf{C}^{(1)} = \mathbf{Z}^{(0)}$, $\tau^{(1)} = 1$, $0 < \mu < 1/L$, k=1

Ensure: $\mathbf{X} = \mu\left(\boldsymbol{\Phi}_{\mathbf{s}} \otimes \mathbf{I}_{\mathbf{3}}\right)^T \mathbf{L}^T \left(\mathbf{Y} - \mathbf{L}\left(\boldsymbol{\Phi}_{\mathbf{s}} \otimes \mathbf{I}_{\mathbf{3}}\right)\mathbf{C}\boldsymbol{\Phi}_{\mathbf{t}}\right)\boldsymbol{\Phi}_t^H$

Estimate the Lipschitz constant L with the power iteration method.

while $\left\|\mathbf{Z}^k - \mathbf{Z}^{k-1}\right\|_F / \left\|\mathbf{Z}^{k-1}\right\|_F > tolerance$ **do**

$\mathbf{Z}^k = prox_{\ell_{21}+\ell_1}\left(\mathbf{C}^k + \mathbf{X}^k, \lambda_s, \lambda_t\right)$

$\tau^{k+1} = \frac{1+\sqrt{1+4\tau^{(k)^2}}}{2}$

$\mathbf{C}^{k+1} = \mathbf{Z}^{(k)} + \frac{\tau^{(k)}-1}{\tau^{(k)}}\left(\mathbf{Z}^{(k)} - \mathbf{Z}^{(k-1)}\right)$

end

B. DERIVING PRIOR FROM FMRI

In this section, we describe a genetic method to derive prior source weighting $\mathbf{w} = \left[w_1, w_2, \cdots w_{N_d}\right]$ for FIST from fMRI data, the prior weighting may provide prior source

location information. It consists of several steps: (i) analysis the preprocessed fMRI data with the General Linear Model (GLM) framework to obtain a statistical parameter map (SPM); (ii) define a threshold for the SPM to get discrete and local contiguous clusters; (iii) project the ''clusters'' onto the cortical mesh. These steps are summarized in Fig. 1.

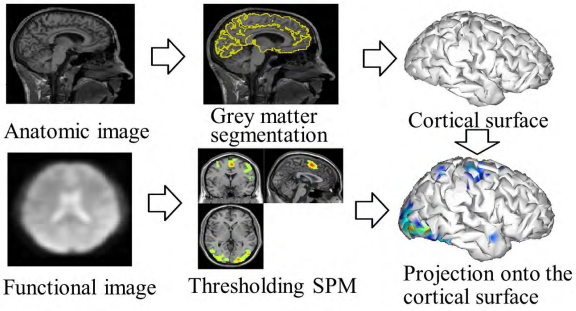

FIGURE 1. Derivation of the prior source weighting from fMRI data.

The ''clusters'' definition in this study is similar with [37] and [52]. The exclusion threshold was set to be 0.05 and the cluster size was 20 voxels in this study. Only the voxels with positive values are considered here, as negative values are thought to be modulated oppositely to the experiment conditions [50]. The 3D clusters are projected onto the cortical surface using nearest-neighbor interpolation method. Each dipole in the EEG source space is assigned the t or F values of its nearest-neighbor voxels; the mean value will be used if a dipole has several nearest-neighbor voxels. This process translates the fMRI cluster matrix into $\mathbf{r} \in \mathbb{R}^{N_d \times 1}$ in solution space, where N_d is the number of dipoles. The sources weighting $\mathbf{w}$ is given by

$$\mathbf{w} = \frac{1}{\mathbf{r} + B} \tag{7}$$

In practice, some brain regions are not activated, which result in some elements of $\mathbf{r}$ being zero. Hence, adding a constant B can avoid the element value of $\mathbf{w}$ being Inf.

For the dSPM, the estimation is given by $\mathbf{S}_{dSPM} = \mathbf{R}\mathbf{L}^T \left(\mathbf{L}\mathbf{R}\mathbf{L}^T + \lambda\mathbf{C}\right)^{-1}\mathbf{y}$, where $\mathbf{R} \in \mathbb{R}^{N_d \times N_d}$ is a diagonal matrix, denotes source covariance matrix. The diagonal element value is assigned the t or F values of its nearest-neighbor voxels, the mean value will be used if a dipole has multiple nearest-neighbor voxels. Large values indicate that those locations that are more likely to be active, while small values indicate locations that are less likely to be active.

C. SELECTION OF THE REGULARIZATION PARAMETERS

In practice, selection of the regularization parameters has big challenge. For all methods, it's to control the balance between the error term $\|\mathbf{Y} - \mathbf{L}\mathbf{J}\|^2_{\mathbf{Q}_\varepsilon}$ and the regularization term to avoid overfitting or underfitting. In the present case, the parameter selection is to set λ_s and λ_t. Several fixed ratios were employed in FIST: $\lambda_s : \lambda_t = 60{:}2$, 70:2, 80:2, 90:2. Here, we present only the results which derived from $\lambda_s : \lambda_t = 70{:}2$. For adjusting the balance between the error term and the regularization term, the ground truth in the simulation is used to tune the parameters λ_s and λ_t. Starting with strong regularization $\lambda_s : \lambda_t = 70{:}2$, we then iteratively update them using factors of 0.8 to let the residual variance $\left\|\hat{\mathbf{Y}} - \mathbf{L}\hat{\mathbf{J}}\right\|^2_{\mathbf{Q}_\varepsilon}$ of the estimated sources $\hat{\mathbf{J}}$ matches the residual variance $\|\mathbf{Y} - \mathbf{L}\mathbf{J}\|^2_{\mathbf{Q}_\varepsilon}$ of the simulated sources $\mathbf{J}$. When applying FIST to the real EEG data, the spatial-to-temporal regularization ratio $\lambda_s : \lambda_t$ was set to 90:2. Since the ground truth is unknown, here we used the same strategy as STOUT for the regularization parameters tuning.

III. SIMULATION SETUP AND DATA DESCRIPTION

A. SOURCE SPACE AND LEAD FIELD MATRIX

The cortex surface and head layers (scalp surface, outer skull, and inner skull) were obtained using Brainstorm's (http://neuroimage.usc.edu/brainstorm/) default MRI, which is derived from an MNI/Colin27 brain using FreeSurfer (http://www.freesurfer.net/). The source space was then generated by down-sampling the cortical surface mesh to a total 6,002 nodes. In the current study, we assumed that the orientation of the source was unknown, and thus, each dipole had three free directions. The forward model which assessed the contribution of every dipolar source to EEG sensors was computed using the Boundary Element Method (BEM) [54]. The lead field matrix $\mathbf{L}$ was calculated using a three-layer BEM model, which consisted of the brain, skull, and scalp surface (conductivity: 1 S/m, 0.0125 S/m, 1 S/m; number of vertices: 642, 642, 1082.), based on the sensor configuration in the 128-channel ActiveTwo system. The forward model and lead field matrix computation were performed using the OpenMEEG implemented in the Brainstorm with default parameters settings.

B. SIMULATED DATA

To demonstrate the performance of the proposed method, in this section, we generate simulated EEG data. We first randomly selected a seed node on the cortical mesh, before gradually growing it into a patch by adding the nearest node. Gaussian-damped sinusoidal time courses [59] were simulated for each node in the patch using

$$J(t) = \exp\left(-(t-c)^2/2\sigma^2\right) \times \sin(2\pi \times f \times t) \tag{8}$$

where $t = -0.1{:}0.001{:}0.3, f = 17Hz, \sigma = 0.02$, and c varied between 0.1, 0.12, and 0.15 to generate different source time course between different active patches. Simulated noiseless EEG data was then generated as the product between the lead field matrix $\mathbf{L}$ and the source currents $\mathbf{J}$. The sensor noise was randomly generated as Gaussian white noise, whose amplitude was controlled by the signal-to-noise ratio (SNR): $SNR = 10\log\left(P(\mathbf{X})/P(\boldsymbol{\varepsilon})\right)$, where $P(\mathbf{X})$ and $P(\boldsymbol{\varepsilon})$ denoted the power of the signal and the noise, respectively, and were defined as the mean variance across channels. The overall noise was then added to the simulated ERP signal. In our experiments, the following scenarios were tested:

1. A single patch with approximately 15 activated dipoles, located on the right parietal region as shown in Fig. 4 ground truth. The corresponding source time courses are shown in Fig. 5(A). The sensor-level SNR was 5-dB.
2. EEG signals with different SNRs. To evaluate the sensitivity to SNR, one patch sources, under different sensor-level SNRs (e. g. -2, 2, 5, and 10-dB), were simulated.
3. Two patch sources, each with approximately 15 activated dipoles, located on the left Middle Temporal and Precentral Gyrus, as shown in Fig. 7. The correlation coefficient between the sources time course of different active patch was 0.9. The sensor-level SNR was 2-dB.
4. Two patch sources with different correlation coefficients (e.g. 0.2, 0.6, 0. 9) between the source time courses of different active patch. Each had approximately 15 activated dipoles. The sensor-level SNR was 2-dB.

In scenario 1 and 2, the source time courses were simulated based on equation (8), with c $= 0.15$ and $\sigma = 0.02$. In scenarios 3 and 4, for the correlation coefficient 0.9, we used the same signals as in scenario 1 for the dipoles in one of the patch, and introduced a 5-ms delay in another patch. To avoid the potential bias at the patch position, 50 experiments were conducted for each condition, such that the generated cortical patch sources covered most brain regions, including both superficial and deep sources.

C. REAL DATA

1) DATA ACQUISITION

The real EEG and fMRI data used in this study were downloaded from the SPM website publicly available online (http://www.fil.ion.ucl.ac.uk/spm/data/). The dataset was recorded from the same subject with the same experimental paradigm. The experimental paradigm involves randomized presentation of 86 faces and 86 scrambled faces for each run (totally 2 runs) [55]. The EEG data were recorded on a 128-channel ActiveTwo system, and sampled at 2048 Hz. The fMRI data were acquired using a gradient-echo EPI sequence on the Sonata. The source space and lead field matrix were calculated with the way described in ''Source Space and Lead Field Matrix'' section.

2) ANALYSIS OF FACE-PROCESSING TASK EEG AND FMRI DATA

EEG data was preprocessed using the public free software EEGLAB (http://cognitrn.psych.indiana.edu/busey/temp/eeglabtutorial4.301/). It was bandpass filtered at 0.1-40Hz, down-sampled to 1000 Hz and transformed to the average reference. The EEG data was then decomposed into independent components using Independent Component Analysis (ICA) method [56]. The components reflecting muscle activity, eye movements and eye-blink artifacts were visually identified and removed. Since each artifact has its typical topography and wave shape, it is easy to visually identify the artifacts from independent components (see [57] for more details). After excluding the artifacts, the clean EEG signal was reconstructed, and segmented into epochs beginning 100 ms pre-stimulus onset and ending 300 ms post-stimulus onset, a 100 ms pre-stimulus baseline was subtracted from each epoch. Finally, each condition got 172 trials for calculating the ERPs. For source localization, the trials corresponding to the face presentations were averaged to obtain face-processing ERPs. The ERPs exhibited a maximal activity peak approximately 160 ms after the stimulus onset, in accordance with a face-specific ''N170'' [27]. It appeared an enhancement of a negative component at occipito-temporal channels, or enhancement of a positive peak near central channels. These effects are shown as a topography map and times series in Fig. 2.

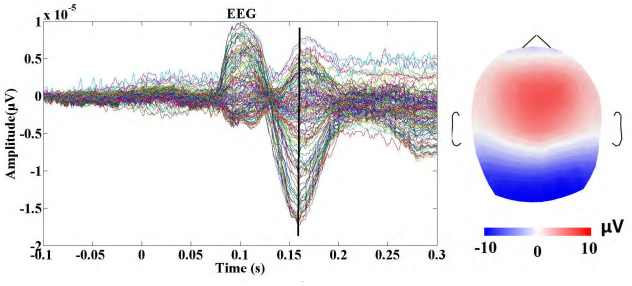

FIGURE 2. Face processing ERP. The topographic map is shown at 160ms after stimulus onset.

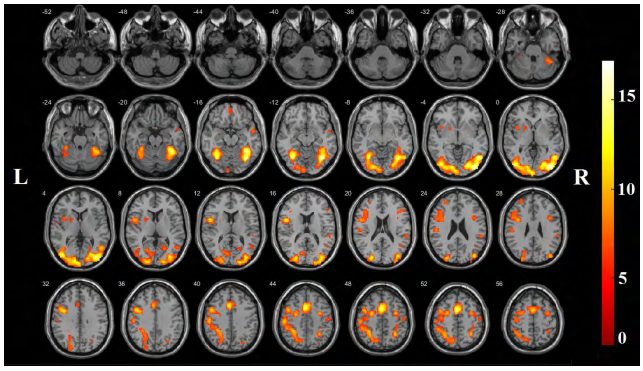

FIGURE 3. Thresholded SPM(T) of face processing in MNI space from one subject.

fMRI data preprocessing and statistical analysis were performed using SPM12, with a conventional preprocessing pipeline including the following: realignment, slice timing correction, normalization, and spatial smoothing. Statistical analysis was performed using the GLM. An SPM of the T-statistic was created, which compared face processing against baseline. This SPM{T} image was then thresholded for regions of at least 10 contiguous voxels, which survived the threshold for a local maxima of $P < 0.05$ (FEW-corrected across the whole brain). Fig. 3 shows the threshold SPM{T} image. The clusters were mainly located at the bilateral midfusiform, bilateral occipital, and medial frontal areas [55].

The clusters in the SPM{T} image were then converted into prior source weighting $\mathbf{w}$ across the 6002 dipolar sources on the cortical mesh, using the previously described steps. Only voxels with a positive value were considered for the conversion. Voxels with negative values were set to zero before the conversion. It should be noted, however, that fMRI prior from a SPM{T} or SPM{F} image that corresponds to a contrast between the responses to faces and scrambled faces stimulations should be used for the source localization analysis of differential ERPs generated from the two types of stimulations.

D. PERFORMANCE METRICS

We used the following three performance metrics to evaluate the performance of the compared source localization methods: the earth mover's distance (EMD) [58], area under the receiver operating characteristic (ROC) curve (AUC) [7], [26], [59], and mean square error (MSE) [59]–[60]. $\hat{\mathbf{J}}$ and $\mathbf{J}$ denote the estimated and simulated current sources, respectively. The energy of the i^{th} simulated and estimated source current were defined as $\mathbf{e}(i) = \sqrt{\left(\mathbf{J}_i^x\right)^2 + \left(\mathbf{J}_i^y\right)^2 + \left(\mathbf{J}_i^z\right)^2}$, $\hat{\mathbf{e}}(i) = \sqrt{\left(\hat{\mathbf{J}}_i^x\right)^2 + \left(\hat{\mathbf{J}}_i^y\right)^2 + \left(\hat{\mathbf{J}}_i^z\right)^2}$. If the energy of the i^{th} dipole source $\mathbf{e}(i) \neq 0$, $\hat{\mathbf{e}}(i) \neq 0$, we consider the i^{th} dipole source is active.

EMD measures the localization error, and a lower EMD value means lower localization error [58]. It's defined as

$$EMD\left(\mathbf{e}, \hat{\mathbf{e}}\right) = \frac{\sum_{i=1}^{m}\sum_{j=1}^{n}\mathbf{F}_{i,j}\mathbf{D}_{i,j}}{\sum_{i=1}^{m}\sum_{j=1}^{n}\mathbf{F}_{i,j}}, 1 \leq m, n \leq N_d \tag{9}$$

where $\mathbf{D}_{i,j}$ is the geodesic distance between the i^{th} simulated source and the j^{th} estimated source, $\mathbf{F}_{i,j}$ denotes the energy cost between the i^{th} simulated source and the j^{th} estimated source, and it can be obtained by minimizing the following overall cost:

$$\mathbf{F}_{i,j}^{*} = \arg\min_{\mathbf{F}_{i,j}} \sum_{i=1}^{m}\sum_{j=1}^{n}\mathbf{F}_{i,j}\mathbf{D}_{i,j}, \quad s.t. \begin{bmatrix} \mathbf{F}_{i,j} \geq 0 \\ \sum_{j=1}^{n}\mathbf{F}_{i,j} \leq \mathbf{e}(i), \quad 1 \leq i \leq m \\ \sum_{i=1}^{m}\mathbf{F}_{i,j} \leq \hat{\mathbf{e}}(j), \quad 1 \leq j \leq n \\ \sum_{i=1}^{m}\sum_{j=1}^{n}\mathbf{F}_{i,j} = \min\left(\sum_{i=1}^{m}\mathbf{e}(i), \sum_{j=1}^{n}\hat{\mathbf{e}}(j)\right) \end{bmatrix} \tag{10}$$

AUC is used to assess the sensibility and specificity of the source estimation [7], [26], [59]. For a chosen threshold $\alpha \in [0, 1]$, if the i^{th} dipole energy $\mathbf{e}(i) > \alpha$, we consider that the i^{th} dipole is active. We can then calculate the true positive (TP), false positive (FP), true negative (TN) and false negative (FN) for each threshold α. If $\hat{\mathbf{e}}(i) \geq \alpha$, $\mathbf{e}(i) \neq 0$, the i^{th} source is TP; if $\hat{\mathbf{e}}(i) \geq \alpha$, $\mathbf{e}(i) = 0$, it's FP; if $\hat{\mathbf{e}}(i) < \alpha$, $\mathbf{e}(i) \neq 0$, it's FN; if $\hat{\mathbf{e}}(i) < \alpha$, $\mathbf{e}(i) = 0$, it's TN. Then, The ROC curves can be generated based on true positive rate (TPR) and false positive rate (FPR):

$$TPR = \frac{TP}{TP + FN}, \quad FPR = \frac{FP}{FP + TN} \tag{11}$$

Since the number of inactive sources (∼10,000) is much larger than the number of active sources (∼100) in our simulations, direct estimate the AUC would have been biased. To circumvent this problem, the procedure in [7], which randomly samples the same number of inactive sources as active sources from both close and far fields of simulated patches, was also applied in the current study. The close field is defined as a 10^{th} neighborhood order of simulated active sources, which as denoted by Θ^{10}. The far field denotes the complementary set of Θ^{10}. By choosing the inactive sources from both the close field and far field, we obtain two metrics, i.e., $\text{AUC}_{\text{close}}$ and AUC_{far}. Overestimation or underestimation of the spatial extent of the source would affect $\text{AUC}_{\text{close}}$, and the occurrence of false positive generated far from the simulated patches would reduce the criterion AUC_{far} [7]. The unbiased AUC is then defined by $AUC = \frac{1}{2}(AUC_{close} + AUC_{far})$. To obtain consistent measurements, which are not sensitive to a particular inactive set selection, the above procedure is repeated 50 times. The mean AUC generated over those 50 trials is used to evaluate the detection accuracy [7], [59]. A large AUC value indicates that a method has high detection sensitivity.

MSE is the square error between the normalized estimated and simulated source activity: $MSE = \left\|\hat{\mathbf{J}}^{\dagger} - \mathbf{J}^{\dagger}\right\|_F^2$, where $\hat{\mathbf{J}}^{\dagger} = \hat{\mathbf{J}}/\left\|\hat{\mathbf{J}}\right\|_F$ and $\mathbf{J}^{\dagger} = \mathbf{J}/\|\mathbf{J}\|_F$ are the normalized estimated and simulated sources, respectively [59], [60]. It's used to evaluate the accuracy of the estimated source time course within the simulated patch. A lower MSE value indicates a higher accuracy for a method to reconstruct the time course.

Two-tailed paired t-tests were performed on all conditions in FIST against each of the other compared methods to determine if FIST yields significantly better estimates.

E. THE PRIOR SOURCE WEIGHTING OF SIMULATIONS

The prior source weighting of simulated data at each location i can be written as

$$\mathbf{w}[i] = \frac{1}{\mathbf{e}(i) + B} \tag{12}$$

To ensure that the $\mathbf{w}$ was derived from experimentally realistic fMRI data, the energy of simulated sources at locations that were not activated were varied between five values, corresponding to 100, 80, 50, 10, and 0% of the maximum value of activated source energy, respectively. These non-zero energies of non-active sources provided a mismatch between fMRI and EEG. This is important because the causes of real EEG signals are not exactly the same as those of the fMRI

signal, according to the current literatures [52], [61], [62]. B is a positive random number here. It was set to 1 in the current study.

For the dSPM method, each diagonal element of $\mathbf{R}$ was given by $\mathbf{e}(i)$. While for the energy value of simulated sources at locations that were not activated were set as the same way of FIST. The off-diagonal elements of $\mathbf{R}$ were set to zero.

IV. RESULTS

A. SINGLE PATCH SIMULATION RESULTS

In this section, we investigate the performance of FIST when there is only one patch, and perform a quantitative comparison with traditional L2-norm constraint methods, including LORETA and wMNE, as well as a L21-mixed-norm constraint method STOUT and fMRI informed method dSPM. The source estimations for the above mentioned methods are shown in Fig. 4. We can see that FIST can recover the sources in space with higher fidelity than STOUT, while LORETA and wMNE generate spatially blurred solutions, and dSPM yields scattered sources. Fig. 5(B-F) presents the corresponding time course reconstruction of each method. It shows that the time course reconstruction of FIST and STOUT are relatively similar with the ground truth, while the LORETA, wMNE and dSPM are totally distorted due to the sensitivity to noise.

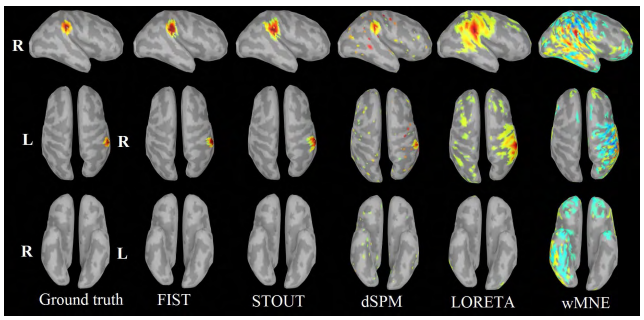

FIGURE 4. The ground truth of one simulated patch with approximately 15 active sources and the estimated results from FIST, STOUT, dSPM, LORETA, and wMNE. Only dipoles with amplitudes larger than 10% of the maximum value are visible.

We also presented the aforementioned performance metrics for all the source localization methods with single patch under 5-dB SNR, as well as other SNRs (i.e., -2, 2, and 10-dB) in Fig. 6. It shows the mean and standard error of the mean (SEM) value for each method. Among the methods, FIST achieves the best performance for MSE at all tested SNRs ($p < 0.001$), and has the best performance of EMD among all the methods ($p < 0.05$) under -2, 2, and 5-dB SNRs. When at 10-dB SNR, FIST has numerically smaller EMD values than STOUT without significance (FIST: 2.068 ± 0.180, STOUT: 2.356 ± 0.151, $p = 0.252$). However, the EMD values in FIST are significantly lower than in the other three methods ($p < 0.001$). FIST also yields significantly higher AUC values than STOUT, LORETA, and wMNE, when the SNR

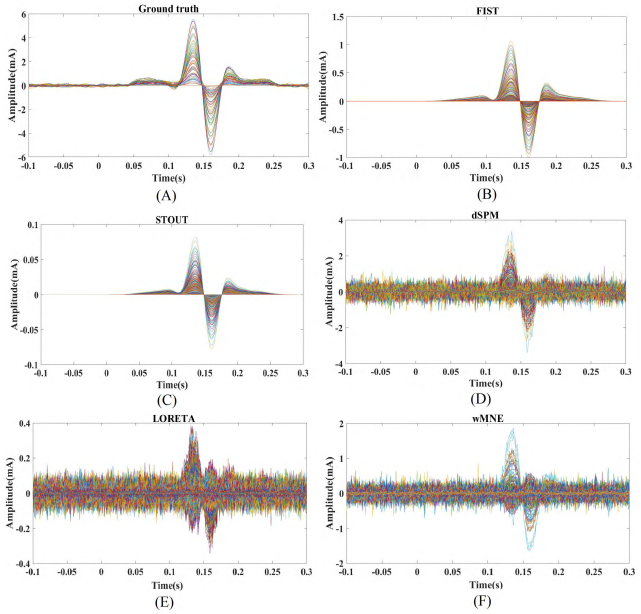

FIGURE 5. The ground truth and the sources time course reconstructions of FIST, STOUT, dSPM, LORETA and wMNE under one simulated patch with 5-dB SNR of sensor noise, the source location of the ground truth and the reconstructed locations by all methods are shown in FIGURE. 4.

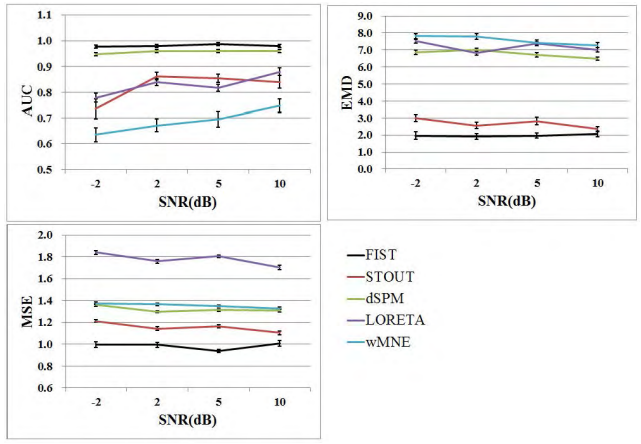

FIGURE 6. Performance metrics for the five source localization methods under one simulated patch with different sensor-level SNRs. The figure includes the results of 50 simulations. Data are shown as Mean ± standard error of mean (SEM).

is -2, 2, and 5-dB ($p < 0.001$). The AUC values generated with FIST are significantly higher than that yielded with dSPM, with an SNR of -2 and 5-dB ($p < 0.001$). It is also numerically higher than that of dSPM under 2 and 10-dB SNRs (2-dB: FIST: 0.980 ± 0.006, dSPM: 0.968 ± 0.006, $p = 0.209$; 10-dB: FIST: 0.977 ± 0.006, dSPM: 0.966 ± 0.006, $p = 0.313$).

B. TWO PATCHES SIMULATIONS RESULTS

To further explore the advantages of FIST, in this section, we apply the same group of methods to the data with two simulated patches. The source estimation results are

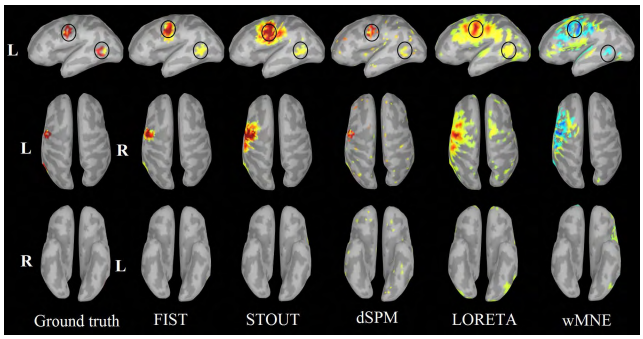

FIGURE 7. The ground truth of two simulated patches with approximately 15 activated sources for each and the estimated results from FIST, STOUT, dSPM, LORETA, and wMNE. The correlation coefficient between the source time courses of different patches is 0. 9. Only dipoles with amplitudes larger than 10% of the maximum value are visible.

shown in Fig. 7. We can see that the estimates by FIST exhibit the closest to ground truth, while STOUT yields over extend sources. LORETA and wMNE cannot clearly detect the true number of the patches due to the spatially blurred reconstruction. Except for the true sources, dSPM also yields scattered sources in other locations.

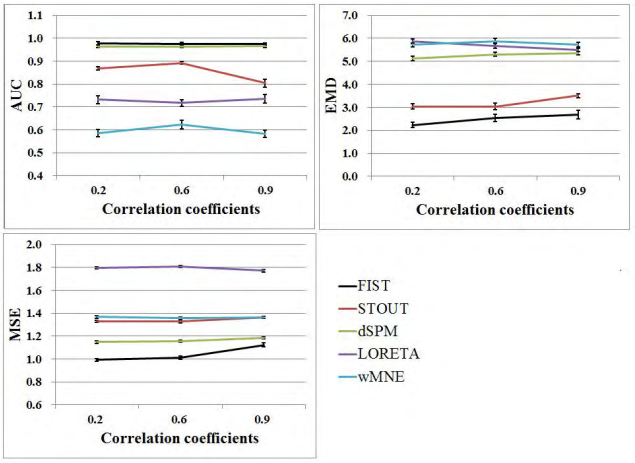

FIGURE 8. Performance metrics for the five source localization methods with three correlation coefficients (i.e., 0.2, 0.6, and 0.9) between two simulated patches. The figure includes the results of 50 simulations. Data are shown as Mean ± standard error of mean (SEM).

In real EEG recordings, activations from two patches are more likely to be different. Thus, correlation between source time courses in different active patch is challenging for source localization. Therefore, we investigated the influence of different correlation coefficients between the time courses of different active patches. Fig. 8 presents the performance metrics of all the methods with three correlation coefficients (i.e., 0.2, 0.6, and 0.9). As the correlation coefficient increases, EMD and MSE values of FIST are increased, while there are only slight changes for AUC. EMD and MSE values of STOUT are also increased as the correlation coefficient increases, but STOUT yields the highest AUC value at correlation coefficient 0.6. EMD values of dSPM are increased as the correlation coefficient increases, while there are only slight changes for AUC and MSE. In contrast, EMD values of LORETA are decreased as the correlation coefficient increases, there are slight changes for AUC and MSE. wMNE provides the highest AUC value at correlation coefficient 0.6, while there are slight changes for EMD and MSE. Among the methods, FIST provides the best performance for EMD and MSE, at all correlation coefficients (EMD: $p < 0.001$; MSE: $p < 0.001$). It has significantly higher AUC values than STOUT, LORETA and wMNE ($p < 0.001$) at all correlation coefficients, and numerically higher AUC values than dSPM without significance (correlation coefficient 0.2: FIST: 0.978 ± 0.007, dSPM: 0.966 ± 0.006, $p = 0.132$; correlation coefficient 0.6: FIST: 0.976 ± 0.007, dSPM: 0.964 ± 0.006, $p = 0.219$; correlation coefficient 0.9: FIST: 0.974 ± 0.006, dSPM: 0.966 ± 0.006, $p = 0.332$).

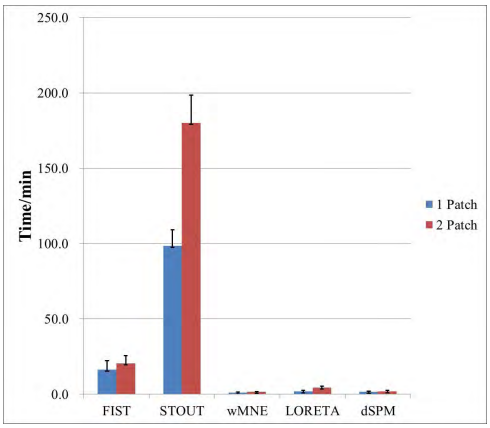

FIGURE 9. Mean Calculation times of FIST, STOUT, wMNE, LORETA and dSPM for one patch and two patches sources (average over the 50 simulations).

All algorithms are implemented in Matlab2012b on a computer with 3.6 GHz Intel Core i7 processor and 8 GB of RAM. The calculation times of the algorithms are shown in Fig. 9. For one patch, FIST only requires about 15 min, STOUT takes nearly 100 min. In addition, when the activated sources are increased (two patches), running FIST takes about 20 min, while executing STOUT takes 150 min longer. LORETA, dSPM and wMNE require less than 5 min for both 1 patch and 2 patch sources.

C. REAL DATA RESULT

In this section, we apply FIST, STOUT, LORETA, wMNE and dSPM to a real EEG data. Fig. 10 presents the source localization results by applying the five methods to the face processing EEG data at 160 ms, in which the left/right and top/bottom view of the cortex are shown for each method. The corresponding reconstructed source time courses for each method are shown in Fig. 11. As shown in Fig. 10, the activations from FIST are mainly localized in the bilateral fusiform gyrus and occipital pole, which corroborate with the results from previous studies [55], [59]. STOUT mainly

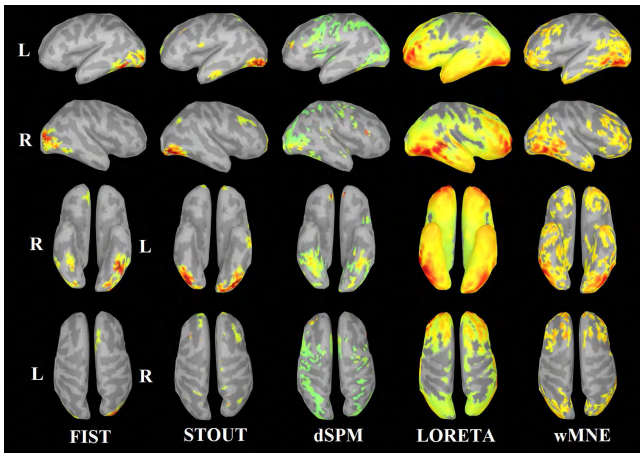

FIGURE 10. Source localization results from FIST, STOUT, dSPM, LORETA and wMNE for face processing EEG, at 160 ms post-stimulation. Only dipoles with amplitudes larger than 10% of the maximum value are visible.

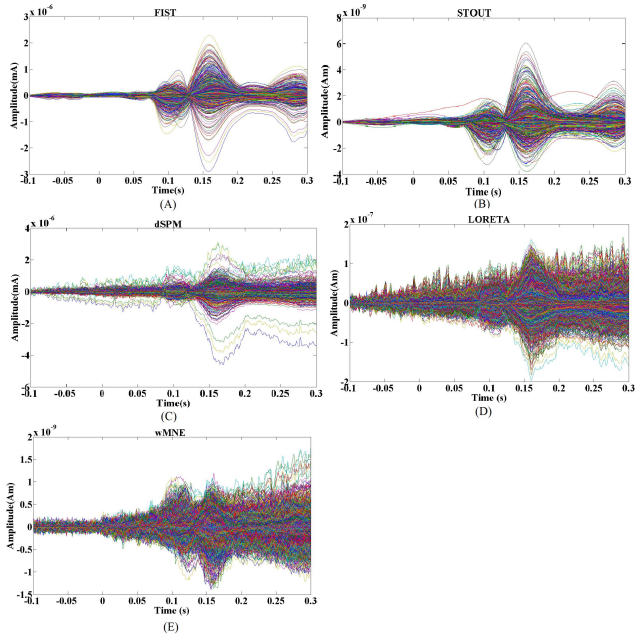

FIGURE 11. The sources time courses estimated by FIST, STOUT, dSPM, LORETA and wMNE for the face processing EEG.

detects activations in the occipital area. dSPM reconstructs source activities in the bilateral fusiform gyrus and occipital pole, sources are also activated in other areas of the brain that are not functional relevant. LORETA and wMNE reveal peak activated sources at the occipital and frontal poles, but the sources around the fusiform area are very widespread.

V. DISCUSSION AND CONCLUSION

In this work, we propose a new EEG-fMRI integration method for EEG source localization. We combine fMRI information as a prior knowledge with a mixed-norm constraint term which defined in terms of time-frequency decomposition of the sources. The well-known FISTA [48], [49] which based on proximal operators is employed for the FIST optimization. And the performance of FIST is discussed with both simulated data, as well as real EEG data from face-processing experiment.

Due to the nature of ill-posed problem, appropriate prior constraint becomes important for achieving optimal and unique solutions in EEG source localization [63]. Previous studies have demonstrated that brain activities may be spatially contiguous [29], [58] and locally homogeneous [27]. The classical LORETA [17] and wMNE methods [16], which based on the L2-norm penalty, produce fuzzy estimates with low spatial resolution (Fig. 4), and leads to non-smooth time courses (Fig. 5 E-F). In particular, we have shown that they may not be able to clearly distinguish multi-patch sources (Fig. 7). Another type of method is to use sparse constraint, including L1-norm [20] and sparsity-inducing norm constraint [21], [22]. As previous studies report, sparse constrained methods may produce over focal estimates, which mean that the estimated activations cover fewer cortical regions than actual sources [64]. An important property of FIST is that leverage spatial basis functions and L21-mixed-norm constraint, which can promote spatially sparse and temporally smooth activations [48]. In this sense, FIST presents better estimation in both space (with better EMDs and AUCs) and time (with better MSEs) compared with LORETA and wMNE which use spatial-only constraint.

fMRI, which is another kind of neuroimaging technique with high spatial resolution [37], [46], is powerful for providing prior information for EEG source localization. For FIST and dSPM [39], although both use prior information provided by fMRI, we note that FIST performed better than dSPM (see Fig. 6 and 8). The estimation of dSPM is more dependent on fMRI than FIST, as illustrated in Fig. 4 and 7. The dSPM has some scattered activations except for the true locations, these scattered locations are false active sources, but their prior weighting values $\mathbf{R}_{i,i}$ are not zeros. In addition, the dSPM estimation with real EEG data (Fig. 10) has almost the same active locations with fMRI. In contrast, FIST can avoid false active source, as shown in Figs. 4 and 7. Meanwhile, the estimated sources of FIST from real EEG data are mainly located at the bilateral fusiform gyrus and occipital pole. These results are consistent with previous studies [55], [59].

As expected, the prior source weighting $\mathbf{w}$ in FIST can help improve computational efficiency. Because each source has its own weight, as previously mentioned, one with small weight is likely to be the candidate source. When the model parameters are optimized, if the prior weighting of a source is bigger, the time-frequency coefficient is closer to zero. As such, the source amplitude also closes to zero. In this sense, the source (or location) without fMRI activation or with negative activation has big prior weighting. It helps reduce the number of candidate sources, which means it decreases the solution space of the source localization problem. Hence, FIST has fewer candidate sources than STOUT [34], which saving a great deal of computational time during optimization (Fig. 9).

As described above, the prior source weighting scheme derived from fMRI data is the key to promote method efficiency. In equation (7), the constant B modulates the strength of prior source weight. The smaller the value of B, the stronger the weight of source. Previous studies have reported that BOLD signals can be directly or indirectly related to neural activity [60]–[62]. The currents that generate EEG are roughly synchronous with BOLD signals [52]. However, there is no evidence demonstrated that EEG and fMRI signals are exactly generated by the same brain area when a cognitive task is being processed [61], [62], [65]. Therefore, if the value of B is too small, the regularization for the corresponding source would be too strong, which leading the source estimation depends on the prior fMRI information too much. Nevertheless, the scheme we proposed in equation (7) can avoid this issue. The weight of one source (or location) without positive fMRI activation was set to 1. In this case, the regularization strength would not be changed.

The mismatch between EEG-fMRI, which is caused by the highly different temporal and spatial scales at which each are generated and collected, poses a challenge to any EEG-fMRI integration analysis. However, it was previously reported that fMRI BOLD signals correlate with local field potentials [66]. Further, they were also correlated with neuronal activity with different frequency bands, both at resting state [61], [67] and during a cognitive task [68]. Based on this evidence, it was reasonable that our inverse scheme, in which the fMRI priors were added as source weighting, only partial corresponded to the fMRI BOLD signals.

In conclusion, this paper proposes a new fMRI informed EEG source localization method FIST, which employs a mixed norm constraint defined in terms of time-frequency decomposition of the sources, and combines the fMRI prior with it. The designed simulated and real EEG data demonstrate that FIST has the superiority in spatio-temporal source recovery ability. By leveraging fMRI information as a prior, FIST improves the source spatial estimation and computational efficiency. In addition, FIST has a potential ability to select the source prior to get better estimation, without totally depending on fMRI information. Therefore, FIST proves to be a promising EEG source localization method for investigating various cognitive tasks and neurological disorders. In the future, we will consider incorporate other neuro image modalities, such as sMRI [69] or diffusion tensor imaging (DTI) [70] in this model. We will also apply the proposed method to analysis of brain networks.

REFERENCES

[1] J. W. Phillips, R. M. Leahy, and J. C. Mosher, "MEG-based imaging of focal neuronal current sources," *IEEE Trans. Med. Imag.*, vol. 16, no. 3, pp. 338–348, Jun. 1997.

[2] J. X. Tao, A. Ray, S. Hawes-Ebersole, and J. S. Ebersole, "Intracranial EEG substrates of scalp EEG interictal spikes," *Epilepsia*, vol. 46, no. 5, pp. 669–676, May 2005.

[3] S. Baillet, J. C. Mosher, and R. M. Leaby, "Electromagnetic brain mapping," *IEEE Signal Process. Mag.*, vol. 18, no. 6, pp. 14–30, Nov. 2001.

[4] M. Hämäläinen, R. Hari, R. J. Ilmoniemi, J. Knuutila, and O. V. Lounasmaa, "Magnetoencephalography—Theory, instrumentation, and applications to noninvasive studies of the working human brain," *Rev. Modern Phys.*, vol. 65, no. 2, pp. 413–497, Apr. 1993.

[5] H. Becker *et al.*, "SISSY: An efficient and automatic algorithm for the analysis of EEG sources based on structured sparsity," *NeuroImage*, vol. 157, no. 1, pp. 157–172, Aug. 2017.

[6] H. Adeli, Z. Zhou, and N. Dadmehr, "Analysis of EEG records in an epileptic patient using wavelet transform," *J. Neurosci. Methods*, vol. 123, no. 1, pp. 69–87, Feb. 2003.

[7] C. Grova, J. Daunizeau, J.-M. Lina, C. Bénar, H. Benali, and J. Gotman, "Evaluation of EEG localization methods using realistic simulations of interictal spikes," *NeuroImage*, vol. 29, no. 3, pp. 734–753, Feb. 2006.

[8] J. M. Palva, S. Monto, S. Kulashekhar, and S. Palva, "Neuronal synchrony reveals working memory networks and predicts individual memory capacity," *Proc. Nat. Acad. Sci. USA*, vol. 107, no. 16, pp. 7580–7585, Nov. 2010.

[9] Z. Dai *et al.*, "EEG cortical connectivity analysis of working memory reveals topological reorganization in theta and alpha bands," *Frontiers Human Neurosci.*, vol. 11, p. 00237, May 2017.

[10] J. D. Lépez, V. Litvak, J. Espinosa, K. Friston, and G. R. Barnes, "Algorithmic procedures for Bayesian MEG/EEG source reconstruction in SPM," *NeuroImage*, vol. 84, pp. 476–487, Jan. 2014.

[11] S. Supek and C. J. Aine, "Simulation studies of multiple dipole neuromagnetic source localization: model order and limits of source resolution," *IEEE Trans. Biomed. Eng.*, vol. 40, no. 6, pp. 529–540, Jul. 1993.

[12] R. Grech, T. Cassar, J. Muscat, K. P. Camilleri, S. G. Fabri, and M. Zervakis, "Review on solving the inverse problem in EEG source analysis," *J. Neuroeng. Rehabil.*, vol. 5, p. 25, Nov. 2008.

[13] I. F. Gorodnitsky, J. S. George, and B. D. Rao, "Neuromagnetic source imaging with FOCUSS: A recursive weighted minimum norm algorithm," *Electroencephalogr. Clin. Neurophysiol.*, vol. 95, no. 4, pp. 231–251, Oct. 1995.

[14] M. Sato *et al.*, "Hierarchical Bayesian estimation for MEG inverse problem," *NeuroImage*, vol. 23, no. 3, pp. 806–826, Nov. 2004.

[15] M. S. Hämäläinen and R. J. Ilmoniemi, "Interpreting magnetic fields of the brain: Minimum norm estimates," *Med. Biol. Eng. Comput.*, vol. 32, no. 1, pp. 35–42, Jan. 1994.

[16] D. H. Brooks, G. F. Ahmad, R. S. MacLeod, and G. M. Maratos, "Inverse electrocardiography by simultaneous imposition of multiple constraints," *IEEE Trans. Biomed. Eng.*, vol. 46, no. 1, pp. 3–18, Jan. 1999.

[17] R. D. Pascual-Marqui, C. M. Michel, and D. Lehmann, "Low resolution electromagnetic tomography: A new method for localizing electrical activity in the brain," *Int. J. Psychophysiol.*, vol. 18, no. 1, pp. 49–65, Oct. 1994.

[18] R. D. Pascual-Marqui. (Oct. 2007). "Discrete, 3D distributed, linear imaging methods of electric neuronal activity. Part 1: Exact, zero error localization." [Online]. Available: https://arxiv.org/abs/0710.3341

[19] R. D. Pascual-Marqui, "Standardized low-resolution brain electromagnetic tomography (sLORETA): Technical details," *Methods Find Exp. Clin. Pharmacol.*, vol. 24, no. Suppl D, pp. 5–12, 2002.

[20] L. Ding and B. He, "Sparse source imaging in electroencephalography with accurate field modeling," *Human Brain Mapping*, vol. 29, no. 9, pp. 1053–1067, Sep. 2008.

[21] S. Saha, F. de Hoog, Y. I. Nesterets, R. Rana, M. Tahtali, and T. E. Gureye. (Jan. 2015). "Sparse Bayesian learning for EEG source localization." [Online]. Available: https://arxiv.org/abs/1501.04621

[22] K. Friston *et al.*, "Multiple sparse priors for the M/EEG inverse problem," *NeuroImage*, vol. 39, no. 3, pp. 1104–1120, Feb. 2008.

[23] F. Costa, H. Batatia, T. Oberlin, C. D'Giano, and J.-Y. Tourneret, "Bayesian EEG source localization using a structured sparsity prior," *NeuroImage*, vol. 144, pp. 142–152, Jan. 2017.

[24] A. Sohrabpour, Y. Lu, G. Worrell, and B. He, "Imaging brain source extent from EEG/MEG by means of an iteratively reweighted edge sparsity minimization (IRES) strategy," *NeuroImage*, vol. 142, pp. 27–42, Nov. 2016.

[25] A. Gramfort, D. Strohmeier, J. Haueisen, M. S. Hämäläinen, and M. Kowalski, "Time-frequency mixed-norm estimates: Sparse M/EEG imaging with non-stationary source activations," *NeuroImage*, vol. 70, no. 15, pp. 410–422, Apr. 2013.

[26] K. Liu, Z. L. Yu, W. Wu, Z. Gu, and Y. Li, "STRAPS: A fully data-driven spatio-temporally regularized algorithm for M/EEG patch source imaging," *Int. J. Neural Syst.*, vol. 25, no. 4, p. 1550016, Jun. 2015.

[27] N. J. Trujillo-Barreto, E. Aubert-Vázquez, and W. D. Penny, "Bayesian M/EEG source reconstruction with spatio-temporal priors," *NeuroImage*, vol. 39, no. 1, pp. 318–335, Jan. 2008.

[28] F. Darvas, U. Schmitt, A. K. Louis, M. Fuchs, G. Knoll, and H. Buchner, "Spatio-temporal current density reconstruction (stCDR) from EEG/MEG-data," *Brain Topography*, vol. 13, no. 3, pp. 195–207, Mar. 2001.
[29] C. Lamus, M. S. Hämäläinen, S. Temereanca, E. N. Brown, and P. L. Purdon, "A spatiotemporal dynamic distributed solution to the MEG inverse problem," *NeuroImage*, vol. 63, no. 2, pp. 894–909, Nov. 2012.
[30] I. Clark, R. Biscay, M. Echeverría, and T. Virués, "Multiresolution decomposition of non-stationary EEG signals: A preliminary study," *Comput. Biol. Med.*, vol. 25, no. 4, pp. 373–382, Jul. 1995.
[31] C. Plummer, A. S. Harvey, and M. Cook, "EEG source localization in focal epilepsy: Where are we now?" *Epilepsia*, vol. 49, no. 2, pp. 201–218, Feb. 2008.
[32] S. R. Liyanage, C. Guan, H. Zhang, K. K. Ang, J. X. Xu, and T. H. Lee, "Dynamically weighted ensemble classification for non-stationary EEG processing," *J. Neural Eng.*, vol. 10, no. 3, p. 036007, Apr. 2013.
[33] S. L. G. Andino, R. G. de Peralta Menendez, C. M. Lantz, O. Blank, C. M. Michel, and T. Landis, "Non-stationary distributed source approximation: An alternative to improve localization procedures," *Human Brain Mapping*, vol. 14, no. 2, pp. 81–95, Oct. 2001.
[34] S. Castaño-Candamil, J. Höhne, J. D. Martínez-Vargas, X.-W. An, G. Castellanos-Domínguez, and S. Haufe, "Solving the EEG inverse problem based on spaceâĂŞtimeâĂŞfrequency structured sparsity constraints," *NeuroImage*, vol. 118, pp. 598–612, Sep. 2015.
[35] S. Haufe *et al.*, "Large-scale EEG/MEG source localization with spatial flexibility," *NeuroImage*, vol. 54, no. 2, pp. 851–859, Jan. 2011.
[36] W. Ou, A. Nummenmaa, J. Ahveninen, J. W. Belliveau, M. S. Hämäläinen, and P. Golland, "Multimodal functional imaging using fMRI-informed regional EEG/MEG source estimation," *NeuroImage*, vol. 52, no. 1, pp. 97–108, Aug. 2010.
[37] R. N. Henson, G. Flandin, K. J. Friston, and J. Mattout, "A parametric empirical Bayesian framework for fMRI-constrained MEG/EEG source reconstruction," *Human Brain Mapping*, vol. 31, no. 10, pp. 1512–1531, Oct. 2010.
[38] X. Lei, P. Xu, C. Luo, J. Zhao, D. Zhou, and D. Yao, "fMRI functional networks for EEG source imaging," *Human Brain Mapping*, vol. 32, no. 7, pp. 1141–1160, Jul. 2011.
[39] A. M. Dale *et al.*, "Dynamic statistical parametric mapping: Combining fMRI and MEG for high-resolution imaging of cortical activity," *Neuron*, vol. 26, no. 1, pp. 55–67, Apr. 2002.
[40] J. George *et al.*, "Functional neuroimaging by combined MRI, MEG and fMRI," *Human Brain Mapping*, vol. S1, p. 89, Mar. 1995.
[41] S. P. Ahlfors and G. V. Simpson, "Geometrical interpretation of fMRI-guided MEG/EEG inverse estimates," *NeuroImage*, vol. 22, no. 1, pp. 323–332, May 2004.
[42] B. R. Cottereau, J. M. Ales, and A. M. Norcia, "Increasing the accuracy of electromagnetic inverses using functional area source correlation constraints," *Human Brain Mapping*, vol. 33, no. 11, pp. 2694–2713, Nov. 2012.
[43] Z. Liu and B. He, "fMRI-EEG integrated cortical source imaging by use of time-variant spatial constraints," *NeuroImage*, vol. 39, no. 3, pp. 1198–1214, Feb. 2008.
[44] Z. Liu, N. Zhang, W. Chen, and B. He, "Mapping the bilateral visual integration by EEG and fMRI," *NeuroImage*, vol. 46, no. 4, pp. 989–997, Jul. 2009.
[45] T. Yoshioka *et al.*, "Evaluation of hierarchical Bayesian method through retinotopic brain activities reconstruction from fMRI and MEG signals," *NeuroImage*, vol. 42, no. 4, pp. 1397–1413, Oct. 2008.
[46] X. Lei, T. Wu, and P. A. Valdes-Sosa, "Incorporating priors for EEG source imaging and connectivity analysis," *Frontiers Neurosci.*, vol. 9, p. 284, Aug. 2015.
[47] M. J. Rosa, J. Daunizeau, and K. J. Friston, "EEG-fMRI integration: A critical review of biophysical modeling and data analysis approaches," *J. Integr. Neurosci.*, vol. 9, no. 4, pp. 453–476, Dec. 2010.
[48] A. Gramfort, M. Kowalski, and M. Hämäläinen, "Mixed-norm estimates for the M/EEG inverse problem using accelerated gradient methods," *Phys. Med. Biol.*, vol. 57, pp. 1937–1961, Mar. 2012.
[49] A. Beck and M. Teboulle, "A fast iterative shrinkage-thresholding algorithm for linear inverse problems," *SIAM J. Imag. Sci.*, vol. 2, no. 1, pp. 183–202, 2009.
[50] J. Sarvas, "Basic mathematical and electromagnetic concepts of the biomagnetic inverse problem," *Phys. Med. Biol.*, vol. 32, no. 1, pp. 11–22, 1987.
[51] P. L. Søndergaard, B. Torrésani, and P. Balazs, "The linear time frequency analysis toolbox," *Int. J. Wavelets Multiresolution Anal. Inf.*, vol. 10, no. 4, p. 1250032, Jul. 2012.
[52] X. Lei, J. Hu, and D. Yao, "Incorporating fMRI functional networks in EEG source imaging: A Bayesian model comparison approach," *Brain Topography*, vol. 25, no. 1, pp. 27–38, Jan. 2012.
[53] A. K. Liu, J. W. Belliveau, and A. M. Dale, "Spatiotemporal imaging of human brain activity using functional MRI constrained magnetoencephalography data: Monte Carlo simulations," *Proc. Nat. Acad. Sci. USA*, vol. 95, no. 15, pp. 8945–8950, Jul. 1998.
[54] J. C. Mosher and R. M. Leahy, "Source localization using recursively applied and projected (RAP) MUSIC," *IEEE Trans. Signal Process.*, vol. 47, no. 2, pp. 332–340, Feb. 1999.
[55] R. N. Henson, Y. Goshen-Gottstein, T. Ganel, L. J. Otten, A. Quayle, and M. D. Rugg, "Electrophysiological and haemodynamic correlates of face perception, recognition and priming," *Cerebral Cortex*, vol. 13, no. 7, pp. 793–805, 2003.
[56] T. Raduntz, J. Scouten, O. Hochmuth, and B. Meffert, "EEG artifact elimination by extraction of ICA-component features using image processing algorithms," *J. Neurosci. Methods*, vol. 243, pp. 84–93, Mar. 2015.
[57] S. J. Luck, *An Introduction to the Event-Related Potential Technique*. Cambridge, MA, USA: MIT Press, 2005.
[58] S. Haufe, V. V. Nikulin, A. Ziehe, K.-R. Müller, and G. Nolte, "Combining sparsity and rotational invariance in EEG/MEG source reconstruction," *NeuroImage*, vol. 42, no. 2, pp. 726–738, Aug. 2008.
[59] K. Liu, Z. L. Yu, W. Wu, Z. Gu, Y. Li, and S. Nagarajan, "Bayesian electromagnetic spatio-temporal imaging of extended sources with Markov random field and temporal basis expansion," *NeuroImage*, vol. 139, pp. 385–414, Oct. 2016.
[60] D. Strohmeier, Y. Bekhti, J. Haueisen, and A. Gramfort, "The iterative reweighted mixed-norm estimate for spatio-temporal MEG/EEG source reconstruction," *IEEE Trans. Med. Imag.*, vol. 35, no. 10, pp. 2218–2228, Oct. 2016.
[61] Z. Zhan *et al.*, "The contribution of different frequency bands of fMRI data to the correlation with EEG alpha rhythm," *Brain Res.*, vol. 1, pp. 235–243, Jan. 2014.
[62] B. R. Cottereau, J. M. Ales, and A. M. Norcia, "How to use fMRI functional localizers to improve EEG/MEG source estimation," *J. Neurosci. Methods*, vol. 250, pp. 64–73, Jul. 2015.
[63] M. Zhu, W. Zhang, D. L. Dickens, and L. Ding, "Reconstructing spatially extended brain sources via enforcing multiple transform sparseness," *NeuroImage*, vol. 86, pp. 280–293, Feb. 2014.
[64] B. He, L. Yang, C. Wilke, and H. Yuan, "Electrophysiological imaging of brain activity and connectivity—Challenges and opportunities," *IEEE Trans. Biomed. Eng.*, vol. 58, no. 7, pp. 1918–1931, Jul. 2011.
[65] F. Xie, L. Xu, Z. Long, L. Yao, and X. Wu, "Functional connectivity alteration after real-time fMRI motor imagery training through self-regulation of activities of the right premotor cortex," *BMC Neurosci.*, vol. 16, p. 29, May 2015.
[66] A. Shmuel, M. Augath, A. Oeltermann, and N. K. Logothetis, "Negative functional MRI response correlates with decreases in neuronal activity in monkey visual area V1," *Nature Neurosci.*, vol. 9, pp. 569–577, Mar. 2006.
[67] D. Mantini, M. G. Perrucci, C. Del Gratta, G. L. Romani, and M. Corbetta, "Electrophysiological signatures of resting state networks in the human brain," *Proc. Nat. Acad. Sci. USA*, vol. 104, no. 32, pp. 13170–13175, Aug. 2007.
[68] S. Hanslmayr, G. Volberg, M. Wimber, M. Raabe, M. W. Greenlee, and K. T. Bauml, "The relationship between brain oscillations and BOLD signal during memory formation: A combined EEG-fMRI study," *J. Neurosci.*, vol. 31, no. 44, pp. 15674–15680, Nov. 2011.
[69] C. Phillips, M. D. Rugg, and K. J. Friston, "Anatomically informed basis functions for EEG source localization: Combining functional and anatomical constraints," *NeuroImage*, vol. 16, no. 3, pp. 678–695, Jul. 2002.
[70] M. Fukushima, O. Yamashita, T. R. Knösche, and M.-A. Sato, "MEG source reconstruction based on identification of directed source interactions on whole-brain anatomical networks," *NeuroImage*, vol. 105, pp. 408–427, Jan. 2015.

HAILING WANG was born in Xinyang, China, in 1987. She received the B.S. degree in communication engineering from the Nanyang Institute of Technology, China, in 2011, and the M.S. degree from Changzhou University, in 2014. She is currently pursuing the Ph.D. degree in computer application technology at the College of Information Science and Technology, Beijing Normal University.

Her research interests include intelligent signal processing, especially machine learning for neuroimaging data processing.

XU LEI received the B.S. degree in information and computing science and Ph.D. degree in biomedical engineering from the University of Electronic Science and Technology of China, China, in 2005 and 2011, respectively. From 2014 to 2015, he was a Visiting Scholar with the Cognition and Brain Science Unit, University of Cambridge, Cambridge, U.K.

He is currently a Professor with the Faculty of Psychology, Southwest University. His main research interests include sleep and multimodal neural imaging, sleep disorders neuroimaging, and EEG-fMRI simultaneous acquisition and fusion techniques.

ZHICHAO ZHAN received the B.S. degree in electronic information from Sun Yat-sen University, China, in 2005. He is currently pursuing the Ph.D. degree in cognitive neuroscience at the State Key Laboratory of Cognitive Neuroscience and Learning, Beijing Normal University.

His research interests include EEG-fMRI simultaneous acquisition and fusion techniques, intelligent signal processing, especially machine learning for neuroimaging data processing.

LI YAO received the B.S. degree from Beijing Normal University, China, in 1983, and the Ph.D. degree from the Chinese Academy of Science, in 1998.

She is currently a Professor and the Dean of the College of Information Science and Technology of Beijing Normal University. Her main research interests include brain signal processing and neuroimaging data analysis.

XIA WU received the B.S. and M.S. degrees in communication and information systems from the College of Information Science and Technology, Beijing Normal University (BNU), China, in 2001 and 2004, respectively, and the Ph.D. degree in basic psychology from the State Key Laboratory of Cognitive Neuroscience and Learning, BNU, in 2007.

She is currently a Professor with the College of Information Science and Technology, BNU. Her main research interests include intelligent signal processing, especially neuroimaging data analysis.